



HAL
open science

Directivity of horns mounted in finite enclosures: A multimodal formulation

Hao Dong, Jean-Baptiste Doc, Simon Félix

► **To cite this version:**

Hao Dong, Jean-Baptiste Doc, Simon Félix. Directivity of horns mounted in finite enclosures: A multimodal formulation. *Journal of the Acoustical Society of America*, 2024, 155 (3), pp.2270-2279. 10.1121/10.0025389 . hal-04798282

HAL Id: hal-04798282

<https://univ-lemans.hal.science/hal-04798282v1>

Submitted on 22 Nov 2024

HAL is a multi-disciplinary open access archive for the deposit and dissemination of scientific research documents, whether they are published or not. The documents may come from teaching and research institutions in France or abroad, or from public or private research centers.

L'archive ouverte pluridisciplinaire **HAL**, est destinée au dépôt et à la diffusion de documents scientifiques de niveau recherche, publiés ou non, émanant des établissements d'enseignement et de recherche français ou étrangers, des laboratoires publics ou privés.

Directivity of horns mounted in finite enclosures: A multimodal formulation

Hao Dong,^{1,a)}  Jean-Baptiste Doc,²  and Simon Félix¹ 

¹Laboratoire d'Acoustique de l'Université du Mans (LAUM), UMR 6613, Institut d'Acoustique Graduate School (IA-GS), CNRS, Le Mans Université, Avenue Olivier Messiaen, 72085 Le Mans, France

²Laboratoire de Mécanique des Structures et des Systèmes Couplés, Conservatoire National des Arts et Métiers, 2 Rue Conté, 75003 Paris, France

ABSTRACT:

The beamwidth is a primary directivity metric for the design of a constant directivity horn. To date, investigations on this property have predominantly been restricted to the half-space radiation or idealized geometries. This paper examines the beamwidth behavior of an axisymmetric horn mounted in a finite cylindrical enclosure by proposing an elegant multimodal solution to the far-field directivity pattern. The variation of beamwidth is examined for the frequency, dimensions of the enclosure, and shape of the horn. At low frequencies, a fitted model is proposed to precisely depict the intrinsic beam narrowing governed by the enclosure diffraction. The asymptotic behavior of the beamwidth is explored as the flange width increases. In the high-frequency range, the horn profile is a determinant of the directivity characteristics. We report the possibility of extending the bandwidth of a constant directivity horn by leveraging the enclosure diffraction effects. The proposed analytical method is highly accurate and much faster than the finite element method for wideband analysis. It allows for an arbitrary velocity distribution at the mouth of the horn and incorporates idealized flange configurations such as an infinite baffle, a zero-thickness closed baffle, and an infinitely long enclosure as limit cases. © 2024 Acoustical Society of America. <https://doi.org/10.1121/10.0025389>

(Received 2 November 2023; revised 10 February 2024; accepted 5 March 2024; published online 28 March 2024)

[Editor: Andi Petculescu]

Pages: 2270–2279

I. INTRODUCTION

This paper investigates the far-field radiation characteristics of an acoustic horn mounted in a finite cylindrical enclosure using a computationally efficient and accurate multimodal method. Emphasis is put on the dependence of the beamwidth characteristics on the dimensions of the enclosure and the shape of the horn. The beamwidth, also known as the coverage angle, represents an angular region in which the far-field power is primarily distributed. Achieving a frequency-invariant beamwidth is greatly desired for sound reinforcement and home audio systems because it would provide consistent tonal balance for the listening area that the beamwidth encompasses.¹ The far-field directivity of a few idealized radiators have been well established, e.g., infinitely flanged vibrators,^{2,3} zero-thickness vibrating disks,^{4,5} and semi-infinite open-ended waveguides with zero wall thickness.^{6–8} However, the literature on the directivity of finite horn radiators is sparse, despite their practical importance.

One possible cause of this research gap is the numerical challenge posed by fully numerical or hybrid methods, e.g., finite element method (FEM),⁹ boundary element method,¹⁰ and coupled FEM-analytical method.¹¹ Since they do not make use of the intrinsic multimodal structure of guided

waves, the computational burden becomes substantial when dealing with a large number of frequencies and geometric parameters. In contrast, the multimodal admittance method by integrating the matrix Riccati equation^{12–15} offers improved efficiency and accuracy for calculating in-duct sound propagation. Concerning the far-field radiation, the state of the art has been restricted largely to the half-space radiation; for instance, the analysis of beamwidth¹⁶ and the multimodal-based shape optimization.¹⁷ To address some of the limitations, Kolbrek and Svensson¹⁸ proposed a hybrid method that combines the multimodal method with an edge-diffraction model to predict the far-field response of a horn terminated in a finite flange. Their work highlights the significant influence of edge diffraction on directivity. However, the integration of two distinct techniques brings complexity and additional computational cost, especially when allowing for higher-order diffraction. The omission of diffraction by boundaries other than the front flange would also lead to a decrease in accuracy.

The first aim of the paper is to overcome the above numerical difficulties. An analytical solution is proposed to calculate the directivity pattern of a finite horn radiator over a wide frequency range, which builds upon a previous work¹⁹ initially developed for modeling the radiation impedance. The method is extended herein to determine the far-field directivity with minimal additional computational cost. Section II presents the method with a numerical validation.

^{a)}Email: hao.dong@univ-lemans.fr

The sound fields on the enclosure surface, used to formulate the directivity function, are solved by placing the enclosure in a larger waveguide with a perfectly matched layer (PML) on its wall. The resulting algebraic formulation is computationally efficient and suitable for an arbitrary velocity distribution at the mouth of the horn. The propagation inside the horn is solved using the improved multimodal admittance method (IMAM),^{14,15} which is known to have improved accuracy for the internal sound field. Importantly, we report for the first time that this advantage is inherited in the far-field calculation. In addition, we show that a few idealized radiators can be conveniently treated as limit cases of the general configuration.

The second objective of this study is to explore the beamwidth characteristics. Understanding the beam narrowing behavior at low frequencies and the enclosure diffraction effects are of essential importance for the optimal design of a constant directivity horn.^{16,17} In Sec. III, we investigate the beamwidth as a function of frequency, which can be characterized into three regions. We report on how the beamwidth is affected by the flange width, enclosure length, and shape of the horn, and propose a fitted model for predicting its low-frequency behavior. Additionally, we report the potential for decreasing the lower control limit of a constant directivity horn with a finite enclosure.

II. MULTIMODAL FORMULATION OF THE DIRECTIVITY FUNCTION

A. Radiation problem

Consider an axisymmetric horn mounted in a cylindrical enclosure with acoustically rigid walls $S_h, S_0 \setminus S_m, S_a$, and S_L [see Fig. 1(a)]. A source at the throat (input end) of the horn emits a sound wave which, after being transmitted through the horn, radiates into free space with certain directivity. For the sake of simplicity, we assume a planar piston source, so that the problem is axisymmetric, although more general configurations could also be described with the proposed formulation (see the supplementary material).

The beamwidth is defined in the polar plot of the directivity pattern as the included angle between two points at which the magnitude drops by 50% (−6 dB) from the biggest lobe.¹⁶ Due to symmetry, we consider herein the beamwidth as half of the included angle, i.e., $\theta_b \in [0, \pi]$, as exemplified by Fig. 1(b).

The directivity pattern is generally obtained from the Kirchhoff–Helmholtz integral equation, which expresses the sound pressure at any point exterior to a surface enclosing the sound sources: in the far field (the radial distance $R \rightarrow \infty$), the pressure is essentially the product of a radial factor e^{ikR}/R (the time dependence is $e^{-i\omega t}$) and an angular factor termed as the directivity function:²⁰

$$D(\theta) = -\frac{ik}{4\pi} \oint_S e^{-ike_f \cdot \mathbf{x}'} [\mathbf{v}(\mathbf{x}') + p(\mathbf{x}')\mathbf{e}_f] \cdot \mathbf{n} \, dS', \quad (1)$$

with $k = \omega/c$ the wavenumber, c the speed of sound, and \mathbf{x}' a point on the enclosing surface S , with outward directed normal \mathbf{n} . The unit vector \mathbf{e}_f gives the direction of the observation point (R, θ, ϕ) . Note that, due to the axisymmetry of

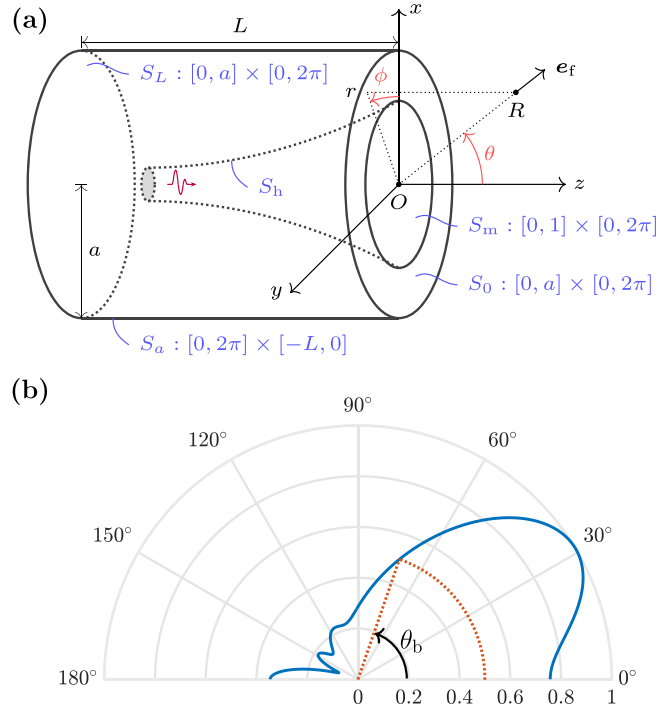


FIG. 1. (Color online) (a) Schematic diagram of a horn mounted in a cylindrical enclosure with radius a and length L . (b) Illustration of the definition of beamwidth.

the problem, the directivity function is independent of azimuth angle ϕ . Also, the fields \mathbf{v} and p are made dimensionless by c and $\rho_0 c^2$, respectively, with ρ_0 the density of air, and the spatial dimensions, including the wavelength $\lambda = 2\pi/k$, are normalized by the radius of the mouth [the circular opening, see Fig. 1(a)].

Upon choosing the surface S as that of the enclosure, and since the normal velocity $\mathbf{v} \cdot \mathbf{n}$ vanishes on the acoustically rigid surfaces $S_0 \setminus S_m, S_a$, and S_L , the directivity function [Eq. (1)] can be decomposed as $D = D_m + D_0 + D_a + D_L$, with

$$D_m(\theta) = -\frac{ik}{4\pi} \iint_{S_m} e^{-ike_f \cdot \mathbf{x}'} v_z(\mathbf{x}') \, dS', \quad (2a)$$

$$D_0(\theta) = -\frac{ik}{4\pi} \iint_{S_0} e^{-ike_f \cdot \mathbf{x}'} p(\mathbf{x}') \mathbf{e}_f \cdot \mathbf{e}_z \, dS', \quad (2b)$$

$$D_a(\theta) = -\frac{ik}{4\pi} \iint_{S_a} e^{-ike_f \cdot \mathbf{x}'} p(\mathbf{x}') \mathbf{e}_f \cdot \mathbf{n} \, dS', \quad (2c)$$

$$D_L(\theta) = -\frac{ik}{4\pi} \iint_{S_L} e^{-ike_f \cdot \mathbf{x}'} p(\mathbf{x}') \mathbf{e}_f \cdot (-\mathbf{e}_z) \, dS'. \quad (2d)$$

Using the integral representations of the Bessel functions of the first kind²¹

$$J_0(x) = \frac{1}{2\pi} \int_0^{2\pi} e^{-ix \cos(\phi' - \phi)} \, d\phi', \quad (3a)$$

$$J_1(x) = \frac{i}{2\pi} \int_0^{2\pi} e^{-ix \cos(\phi' - \phi)} \cos(\phi' - \phi) \, d\phi', \quad (3b)$$

this gives

$$D_m(\theta) = -\frac{ik}{2} \int_0^1 v_z(r', 0) J_0(kr' \sin \theta) r' dr', \quad (4a)$$

$$D_0(\theta) = -\frac{ik \cos \theta}{2} \int_0^a p(r', 0) J_0(kr' \sin \theta) r' dr', \quad (4b)$$

$$D_a(\theta) = -\frac{ka \sin \theta}{2} J_1(ka \sin \theta) \int_{-L}^0 p(a, z') e^{-ikz' \cos \theta} dz', \quad (4c)$$

$$D_L(\theta) = \frac{ik \cos \theta}{2} e^{ikL \cos \theta} \int_0^a p(r', -L) J_0(kr' \sin \theta) r' dr'. \quad (4d)$$

The following step consists now of expressing each of these four contributions to $D(\theta)$ as functions of the velocity field at the mouth, $v_z(r', 0)$, $r' \in [0, 1]$. To do this, we use a multimodal formulation of the exterior field.

B. Multimodal formulation

Given the solutions $\varphi_n(r') = \sqrt{2} J_0(\gamma_n r') / J_0(\gamma_n)$ of the Neumann Laplacian eigenproblem in the unit disk, let \mathbf{u} be the vector of the components of $v_z(r', 0)$ in the orthonormal basis $\{\varphi_n\}$.²² Then, Eq. (4a) can be written

$$D_m(\theta) = -\frac{ik}{2} \mathbf{Y}^T \mathbf{u}, \quad (5)$$

where

$$\mathbf{Y}_n(\theta) \equiv \int_0^1 \varphi_n(r') J_0(kr' \sin \theta) r' dr'. \quad (6)$$

Regarding Eqs. (4b)–(4d), in order to relate the pressure fields $p(r', 0)$, $p(a, z')$, and $p(r', -L)$ to $v_z(r', 0)$, or equivalently to \mathbf{u} , we consider the enclosure as itself embedded in an infinite waveguide with an annular PML on its wall (see Fig. 2). It is then possible to derive algebraic solutions for the exterior field.¹⁹ The pressure field $p(r', z' \geq 0)$ is developed on the basis of eigenfunctions $\varphi_{Bn}(r') = b^{-1} \varphi_n(r'/b)$, with b the radius of the “PML” waveguide:

$$p(r', z' \geq 0) = \boldsymbol{\varphi}_B^T(r') \mathbf{p}^+(z'), \quad (7)$$

so that Eq. (4b) becomes

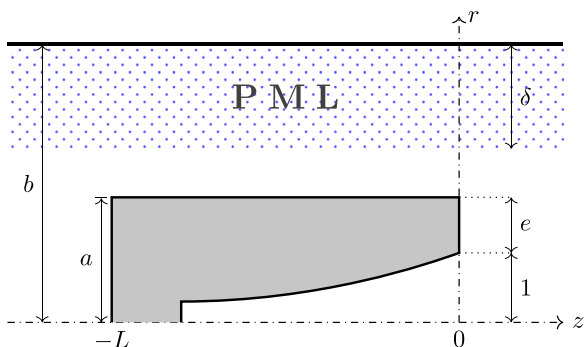


FIG. 2. (Color online) Configuration of the “PML” waveguide.

$$D_0(\theta) = -\frac{ik \cos \theta}{2} \boldsymbol{\kappa}^T \mathbf{p}^+(0), \quad (8)$$

where

$$\kappa_n(\theta) \equiv \int_0^a \varphi_{Bn}(r') J_0(kr' \sin \theta) r' dr'. \quad (9)$$

Now, $\mathbf{p}^+(0)$ in Eq. (8) can be related to \mathbf{u} by writing the continuity of the pressure and velocity field in the plane $z=0$ (see the supplementary material); it translates into a linear relation $\mathbf{p}^+(0) = \mathbf{H}_0 \mathbf{u}$; hence

$$D_0(\theta) = -\frac{ik \cos \theta}{2} \boldsymbol{\kappa}^T \mathbf{H}_0 \mathbf{u}. \quad (10)$$

In the same way, writing

$$p(r', z' \leq -L) = \boldsymbol{\varphi}_B^T(r') \mathbf{p}^-(z') \quad (11)$$

leads to

$$D_L(\theta) = \frac{ik \cos \theta}{2} e^{ikL \cos \theta} \boldsymbol{\kappa}^T \mathbf{p}^-(-L). \quad (12)$$

By writing the continuity of the pressure and velocity fields in the plane $z=-L$ and the propagation in the annular region $[-L, 0]$, we can relate $\mathbf{p}^-(-L)$ to \mathbf{u} : $\mathbf{p}^-(-L) = \mathbf{H}_L \mathbf{u}$ (see the supplementary material). Finally, based on the modal solution of the pressure field in the annular region $[-L, 0]$, we can write

$$D_a(\theta) = -\frac{ka \sin \theta}{2} J_1(ka \sin \theta) \boldsymbol{\varphi}_C^T(a) \mathbf{H}_a \mathbf{u}, \quad (13)$$

where the components $\varphi_{Cn}(r')$ of the column vector $\boldsymbol{\varphi}_C$ are the Neumann eigenmodes in an annulus with radii a and b (see the supplementary material). It follows that the directivity function reads $D(\theta) = \mathbf{f}^T(\theta) \mathbf{u}$, where $\mathbf{f}(\theta)$ is algebraically known. The velocity \mathbf{u} is computed from the piston at the throat using the multimodal admittance method.¹⁵

Solutions for the following extreme geometries can be deduced from the general formulation.

1. Infinite baffle ($e=\infty$)

For a radiator mounted in an infinite rigid baffle, the directivity function is derived from the Rayleigh integral formula:²

$$D(\theta) = 2D_m(\theta) = -ik \mathbf{Y}^T \mathbf{u}, \quad (14)$$

where the factor of 2 arises from the Green’s function that satisfies the Neumann boundary condition on the baffle.

2. Finite closed baffle ($L=0$, one-side radiator)

Mellow and Kärkkäinen⁴ described an analytical expression of the directivity of an oscillating rigid disk in a finite closed circular baffle, also known as a one-side piston

radiator. In our method, setting $L = 0$ provides an alternative solution, while allowing for an arbitrary velocity distribution. Since the sidewall S_a disappears, the directivity function only has contributions from S_0 and S_L .

3. Infinitely long enclosure ($L = \infty$)

The configuration becomes a semi-infinite waveguide with arbitrary wall thickness (including $e = 0$) as considered in previous work.¹⁹ Since the bottom surface S_L disappears, the directivity function only has contributions from S_0 and S_a . Given that there are no reflected waves in the annular region $z \leq 0$, setting the reflection matrix R_L to zero yields the solution. Note that in the limit case of zero wall thickness, rigorous expressions for the modal directivity functions can be derived using the Wiener–Hopf technique.^{23,24}

C. Numerical computation and validation

For the computation, a compact PML with thickness $\delta = b - a$ is employed, filling the entire annular region. The numbers of modes in the annular and circular regions of the “PML” waveguide are chosen according to their transversal dimensions: $N_C/N_B = \delta/b$. The transverse eigen-solutions for the “PML” waveguide (see the supplementary material) are computed once with a sufficiently large number of modes and stored. Subsequently, calculating the modal directivity functions for any frequency and direction involves simple algebraic operations, thereby highly efficient.

The accuracy of the method is first validated against FEM for two horn-loaded enclosures depicted in Fig. 3 (expressions for the horn profile are provided in the supplementary material). The IMAM is used to solve the internal field of the horn, with its advantages elaborated upon later

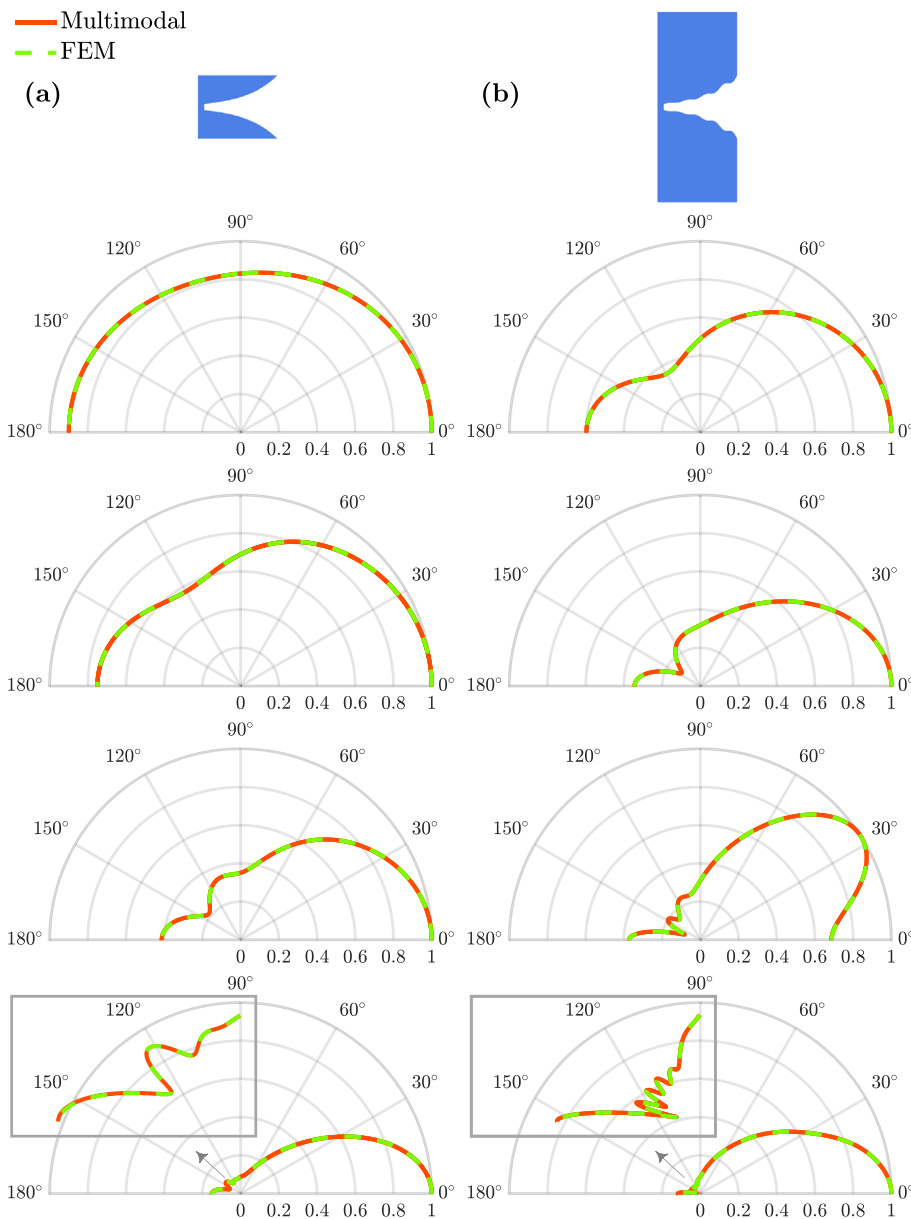


FIG. 3. (Color online) Directivity patterns computed with the multimodal method in comparison with FEM for (a) an exponential horn ($a = 1$) and (b) a wave-shaped exponential horn ($a = 3$). $L = 2.5$, $\delta = 1$, $N_B = 200$, the number of modes within the horn $N_A = 20$. From top to bottom: $k = 0.5, 1, 2, 4$. The insets show the back lobes zoomed by five times.

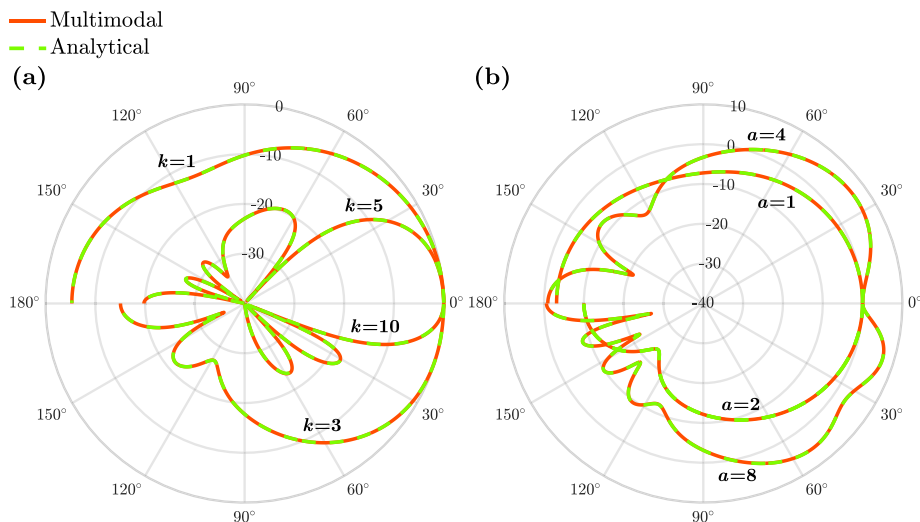


FIG. 4. (Color online) Comparison of the directivity patterns for a one-side radiator between the multimodal method ($\delta = 1, N_B = 200$) and the analytical method proposed by Mellow and Kärkkäinen (Ref. 4) (plotted in dB for the sake of comparison, normalized with respect to 0°). (a) $a = 2$. (b) $k = \pi/2$.

in this section. The directivity patterns are compared for various frequencies. The maximum absolute error is typically between 10^{-4} and 10^{-3} , showing excellent accuracy of the multimodal method. Meanwhile, its computational efficiency notably surpasses the FEM.

The method is also compared against the analytical solution for a one-side radiator.⁴ Figure 4 shows excellent agreement between these two solutions for the geometries and frequencies reported in Ref. 4, Figs. 16 and 17. Good agreement is also observed for a large flange at a low frequency, e.g., $e = a - 1 = 20, k = 0.05$. Note that in the analytical method, the series expansion of the pressure field on the radiator surface is determined by solving an algebraic equation. However, the condition number increases rapidly with the matrix order, especially for large values of ka . Consequently, the use of multiple precision computing is inevitable to obtain an accurate solution at high frequencies. In contrast, the accuracy of the present method is barely degraded as ka increases, facilitating analysis for a broad range of geometries and frequencies.

A supplementary mode is only used for solving the propagation within the horn, which is orthogonal to the standard basis of rigid waveguide modes.¹⁵ A known advantage of IMAM is the

enhanced accuracy in the field solution within the horn.¹⁴ Here, we demonstrate that the far-field solution inherits this improvement due to the precise velocity field at the mouth. The percentage relative error of the directivity function is calculated with respect to the number of modes in the horn (N_A) for comparing the standard and improved bases: $\epsilon(\theta; N_A) = |(D - D_{\text{ref}})/D_{\text{ref}}| \times 100\%$, where D_{ref} is a reference solution calculated using the corresponding basis. In the computation, we fix $N_B = 200$ and $N_{A,\text{ref}} = N_C = N_B/b$. Figures 5(a) and 5(b) illustrate the mean and standard deviation of the error in θ for the two geometries in Fig. 3. Discrepancies of the errors in different directions are insignificant for both methods. However, for a given N_A , the mean error of the improved method is lower than that of the standard method by over 1 order of magnitude. The accuracy achieved by the improved method with several modes surpasses the standard method with tens of modes.

III. ANALYSIS OF BEAMWIDTH

A. Beamwidth in three frequency regions

The section explores the influence of the enclosure dimensions and shape of the horn on the beamwidth

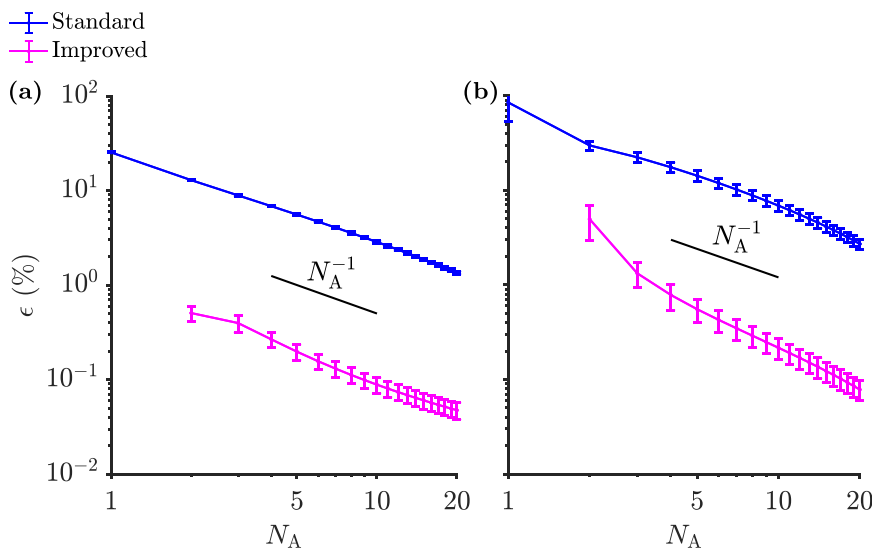


FIG. 5. (Color online) Convergence analysis of the directivity function with standard and improved bases for the geometries shown in Fig. 3: (a) exponential horn, $k = 1$. (b) wave-shaped horn, $k = 4, \delta = 1$.

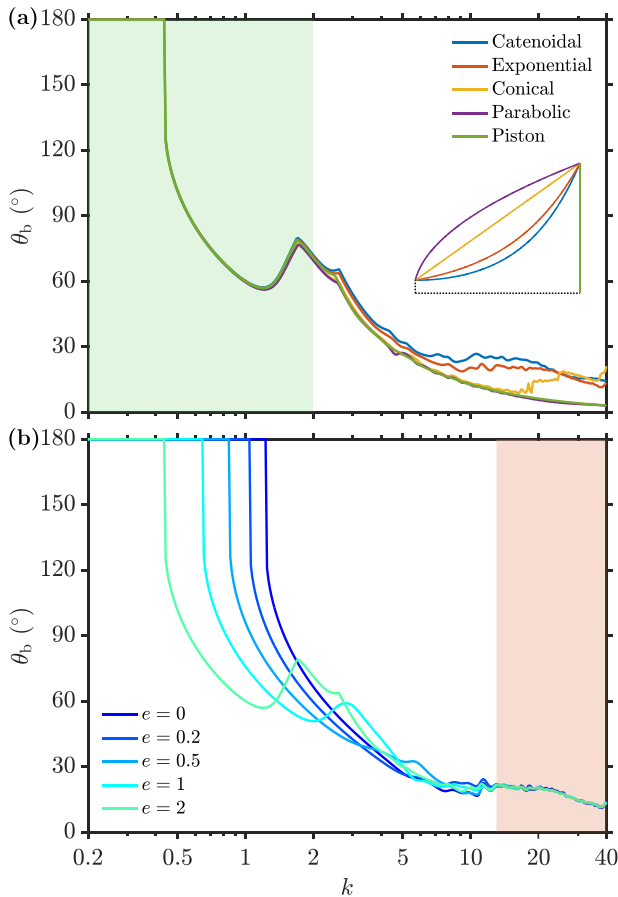


FIG. 6. (Color online) Beamwidth of a horn-loaded enclosure ($L = \infty$) showcasing various horn profiles and flange widths. (a) Flange width of $e = 2$. The insets show the profiles. (b) Exponential horn. The diffraction and propagation control regions are designated by colored background.

characteristics. First, we focus on an infinitely long enclosure ($L = \infty$) to highlight the influence of the lateral dimension, i.e., the flange width $e = a - 1$. Several classical shapes are considered with throat radius $a_t = 0.1$ and length of the horn $L_h = \ln 10$. An exponential horn in this dimension has a cutoff wavenumber of $k_c = 1$, according to the Webster's equation.²⁵ The numbers of modes used to compute the beamwidth are $N_A = 20$ and $N_B = 200$.

At low frequencies, as shown by the shaded area in Fig. 6(a), for a given flange width, the beamwidth (as well as the directivity pattern) is asymptotically independent of the horn profile and can be simply represented by that of a

vibrating piston placed at the mouth; in other words, by the first-order (piston) modal directivity function $f_0(\theta)$. These phenomena are valid for other values of e labeled in Fig. 6(b) as well as finite-length enclosures, indicating that in the long-wavelength limit, directivity is dominated by enclosure diffraction.

Nevertheless, the consistency of beamwidth for various horn shapes does not imply a consistent and near-planar velocity distribution at the mouth. Figure 7 illustrates that the wavefront at the mouth has curvature and varies with the horn profile. The exemplified frequency is lower than the cutoff frequency at the mouth, i.e., $k < \gamma_1 \approx 3.83$. The non-planar wave components at the mouth are evanescent and thus cannot efficiently radiate to the far field,⁸ manifested in the low amplitude of their corresponding modal directivity functions, $|f_n(\theta)| \ll |f_0(\theta)|, \forall n \geq 1$. The mouth wavefront is mainly set by the horn wall angle and hard-wall boundary condition. The catenoidal horn exhibits a more curved wavefront than the parabolic horn. Despite the distinct wavefronts, the beamwidths for the catenoidal and parabolic profiles are close and differ from that of the piston by only 1.8% and 0.6%, respectively.

At high frequencies, as shown by the shaded area in Fig. 6(b), for a given horn profile, the beamwidth is nearly independent of the flange width. This behavior is also observed for other profiles labeled in Fig. 6(a), indicating that in the high-frequency limit, the directivity is largely determined by the in-duct propagation and not influenced by the diffraction. Figure 6(a) also shows that the beamwidth of the parabolic profile is close to that of the piston, implying high axial directivity.²⁶ In the mid-frequency range, both the diffraction and propagation affect the beamwidth. These observations suggest a characterization of the beamwidth into three regions: the (external) diffraction control region, the (in-duct) propagation control region, and the interplay region.

B. Low-frequency model

The diffraction control region is virtually characterized by the first-order (piston) modal directivity function $f_0(\theta)$ [see Fig. 8(a)]. All curves show a monotonic decrease in the low-frequency range following a beamwidth plateau of $\theta_b = \pi$ (for a finite value of e) or $\theta_b = \pi/2$ (for $e = \infty$). To examine this beam narrowing phenomenon, we start with a limit

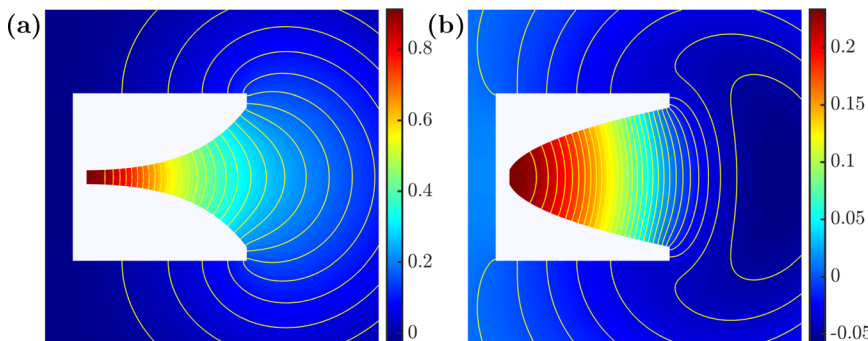


FIG. 7. (Color online) Sound pressure field $\text{Re}(p)$ with contour lines for two enclosures with (a) catenoidal and (b) parabolic horn profiles computed with the multimodal method. The throat velocity $v_z = 1$, $k = 1$, $e = 0.2$, $L = 2.5$. A wider “PML” waveguide with $b = 4.4$ and $\delta = 2$ is used in this example.

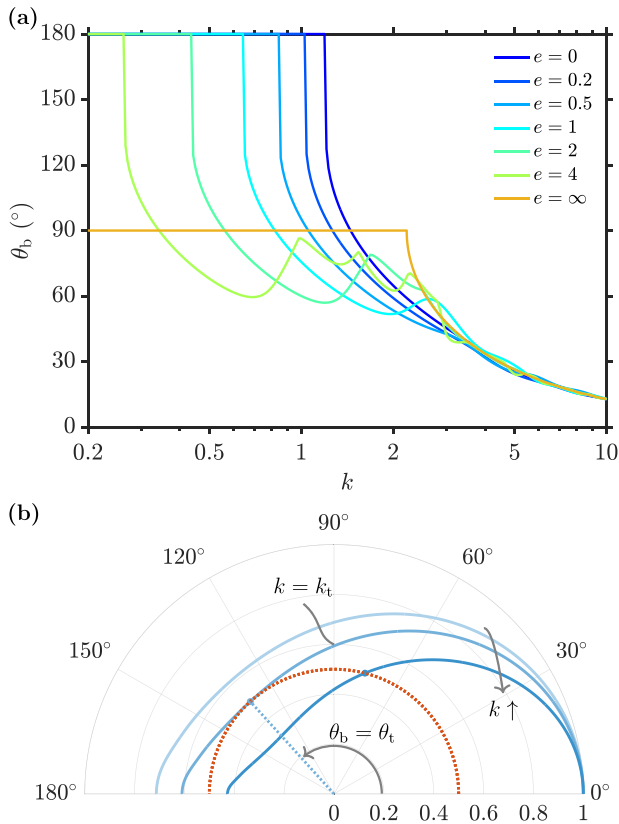


FIG. 8. (Color online) (a) Beamwidth of the piston mode for various flange widths. (b) Directivity patterns for $e=1$ as frequency increases. $k_t \approx 0.65$ is the turning wavenumber.

case of $e = \infty$, for which the directivity function has an analytical expression [see Eq. (6) and the supplementary material]:

$$f_0(\theta) = -ik \frac{\sqrt{2}J_1(k \sin \theta)}{k \sin \theta}, \quad (15)$$

thus giving the beamwidth:

$$\theta_b = \arcsin\left(\frac{k_{t,\infty}}{k}\right), \quad k \geq k_{t,\infty}, \quad (16)$$

where $k_{t,\infty} \approx 2.2$ is a turning wavenumber given by the root of equation $J_1(x)/x = 1/4$, above which θ_b monotonically decreases from $\pi/2$, and the radiation exhibits distinct directivity.

The beamwidth for a finite value of e exhibits a similar but steeper reduction above its turning frequency. To have a better understanding, Fig. 8(b) exemplifies how the directivity pattern varies near the turning frequency (for $e=1$). As frequency increases, the beamwidth θ_b remains as π until the directivity pattern first intersects the -6 dB circle at the turning wavenumber k_t . Moreover, their intersection is tangential at a turning angle $\theta_t < \pi$, that is, the θ_b suddenly drops from π to θ_t , forming a discontinuity.

The dependence of both turning parameters on the flange width e is shown in Fig. 9(a) (open circles). The turning angle is almost independent of e (dashed line),

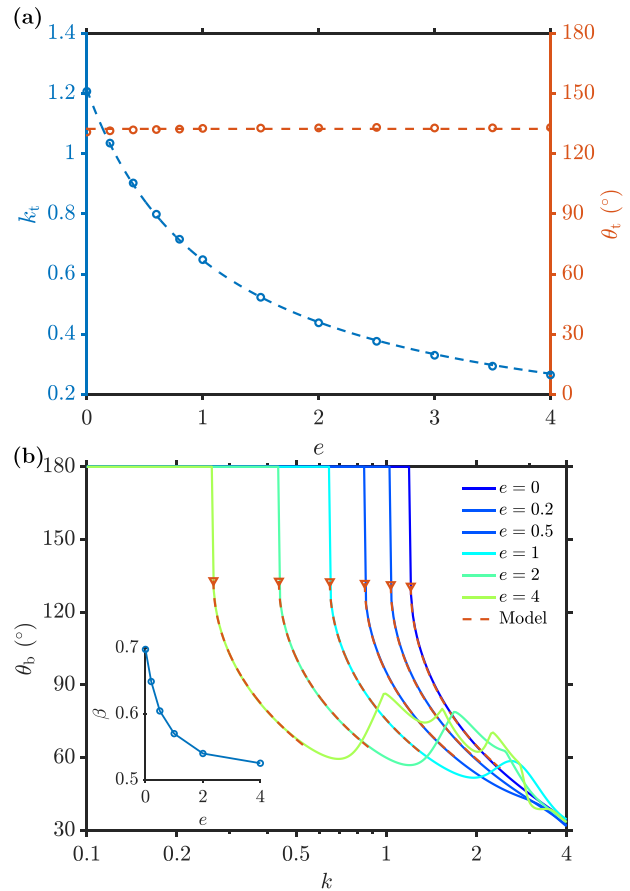


FIG. 9. (Color online) (a) Dependence of the turning parameters (k_t, θ_t) on e . (b) Empirical model for the beamwidth within the monotonic range. The triangle markers show the turning points. The inset shows the dependence of the fitted exponent on e .

$\theta_t \approx 132^\circ$, and the turning wavenumber k_t can be accurately fitted by a rational curve (dashed line):

$$k_t(e) = \frac{1}{1 + \alpha e} k_t(0), \quad (17)$$

where $k_t(0) \approx 1.2142$ and $\alpha \approx 0.8794$. Based on these parameters, we further develop an empirical model for the monotonic decrease in the beamwidth. It takes form of an inverse sine function as Eq. (16) and is modified by an additional fitted exponent β :

$$\theta_b = \arcsin\left[\left(\frac{k_t}{k}\right)^\beta\right] \times \frac{2\theta_t}{\pi}, \quad k > k_t. \quad (18)$$

The first octave band above k_t is used for the fitting. Figure 9(b) shows the validity of the fitted model as well as the exponent β as a function of e . The results show that the low-frequency dropping rate of the beamwidth slows down as the flange becomes larger.

C. Edge diffraction and asymptotic behavior

For a large flange, the beamwidth can exhibit noticeable fluctuations above the monotonic range [see Fig. 8(a)],

which is primarily due to the edge diffraction. Figure 10(a) illustrates how they are associated with the variation of the directivity pattern. The initial monotonic narrowing of the beam ends with a rapid broadening of its mainlobe. Upon reaching the first beamwidth maximum, the energy distribution within 30° is almost uniform. Subsequently, the mainlobe direction deviates from 0° , leaving an on-axis dip in the directivity pattern, accompanied by the narrowing of the beamwidth until the axial mainlobe is restored. The beamwidth curve exhibits non-smoothness at the critical frequencies at which the mainlobe direction shifts because the reference direction for defining the beamwidth jumps here.

As the flange width e increases, the oscillation in beamwidth covers lower frequencies, as shown in Fig. 8(a). An intriguing question is how it eventually converges to a straight line as $e \rightarrow \infty$. Figure 10(b) displays the beamwidth curve for $e = 20$, showing a periodic occurrence of the “M”-shaped pattern observed in Fig. 10(a), the plateau for $e = \infty$ serving as its upper bound. Note also that Eq. (17) remains effective for $e = 20$. The numerically calculated turning

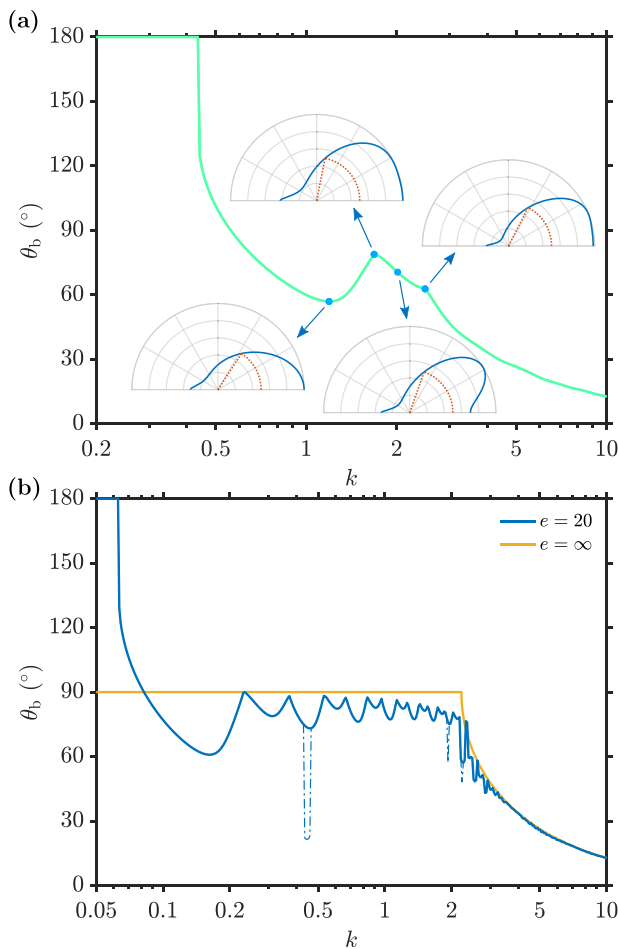


FIG. 10. (Color online) (a) Beamwidth of the piston mode at the mouth for $e = 2$ and directivity patterns at a few representative frequencies. (b) Beamwidth for $e = 20$ compared to $e = \infty$. The beamwidth could occasionally have multiple values, one may select a continuous branch (solid line) to avoid a dip (dashed line) (see the supplementary material for further elucidation).

parameters $(\theta_t, k_t) = (132.7^\circ, 0.06333)$ agree well with the predicted values with an error of less than 5%.

D. Finite-length enclosures

The influence of the enclosure length L on the beamwidth is examined in Fig. 11. For a finite value of L , the back-and-forth reflection along the sidewall S_a and the diffraction by bottom surface S_L bring only minor fluctuations around the beamwidth of $L = \infty$. In terms of the turning parameters, compared to $L = \infty$, the angle θ_t becomes smaller, whereas the wavenumber k_t does not monotonically vary with L .

E. Interplay and propagation control regions

As frequency increases to the interplay and propagation control regions, the shape of the horn can be designed to achieve near-constant directivity, e.g., using empirical formulas¹⁶ or shape optimization.¹⁷ The low-frequency monotonic decrease in the beamwidth sets a lower limit to the control frequency band. For the half-space radiation, the lower frequency limit can be evaluated by equating the beamwidth expression [Eq. (16)] with the target beamwidth value.¹⁶ For horns with a finite flange, this frequency is likely smaller than the half-space case.

This section reports the possibility of extending the control bandwidth by exploiting the diffraction effects. We start with a conical horn, which provides a near-constant coverage angle at high frequencies. For instance, a 120° cone exhibits a controlled beamwidth of $\theta_b \approx 60^\circ$ as shown in Fig. 12(a). When the horn is mounted in an infinite baffle, the lower control frequency is around $k = 3$. By employing

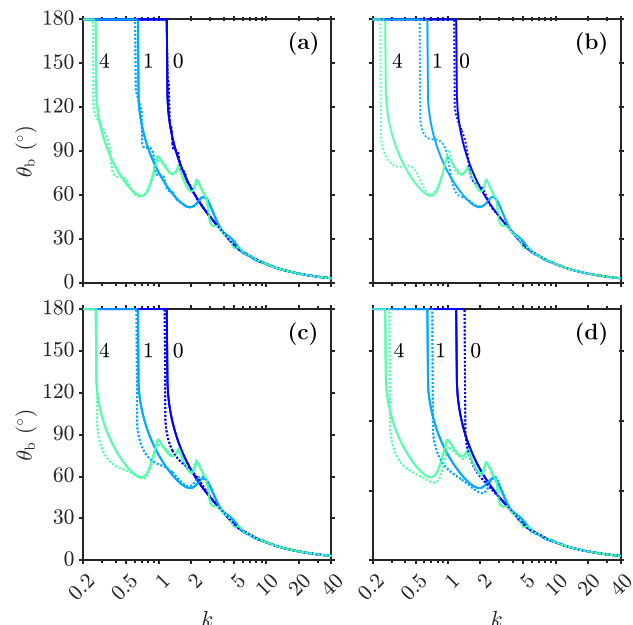


FIG. 11. (Color online) Beamwidth of a piston mounted in a finite-length enclosure. Solid lines: $L = \infty$; dotted lines: (a) $L = 10$, (b) $L = 2.5$, (c) $L = 0.5$, (d) $L = 0$. The numbers designate the values of e .

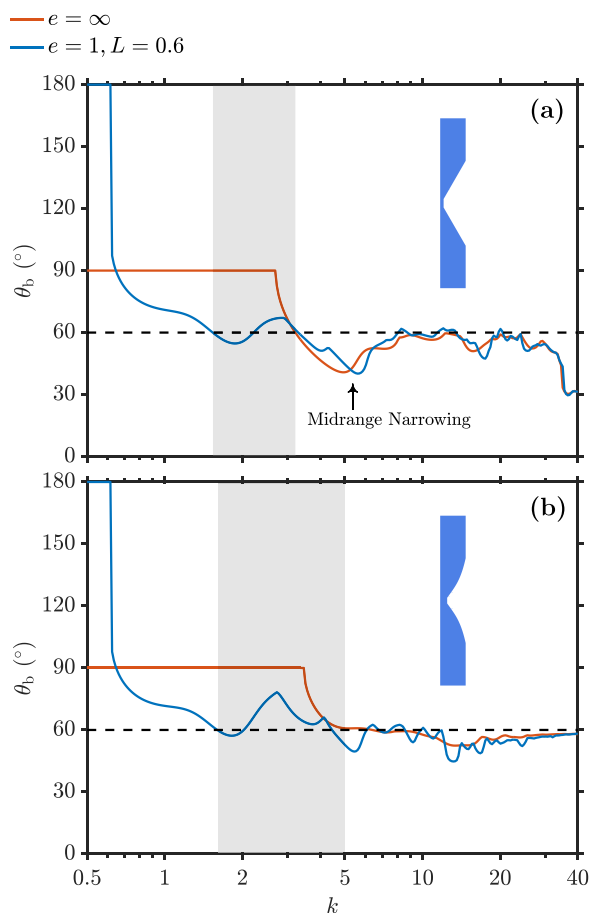


FIG. 12. (Color online) Beamwidth of (a) a conical horn with an included angle of 120° and (b) a constant directivity horn. Shaded areas show extension of the control band.

an enclosure with a flange width of $e=1$ and length of $L=0.6$, the lower control limit is decreased by an octave.

Note that the conical horn has some remarkable drawbacks that stem from a sudden change of wavefront at the mouth.¹⁶ One of them is the so-called midrange narrowing shown in Fig. 12(a). A measure to mitigate this defect is to increase the flaring rate near the mouth, equivalently shading the mouth velocity distribution in the mouth plane. One empirical approach to modifying the conical shape is to add a term in its expression, $r = a_0 + a_1z + a_nz^n$, known as a bi-radial design.²⁷ The procedure to determine these coefficients is detailed in the supplementary material. Figure 12(b) shows that the midrange narrowing is largely attenuated for both cases, while the lower control frequency of the finite enclosure remains at $k \approx 1.6$.

IV. CONCLUDING REMARKS

A closed-form solution of modal directivity functions for a circular vibrator on a finite cylinder is presented and combined with the IMAM to analyze the far-field radiation of a horn-loaded enclosure. For a given flange width, the transverse eigenvalue problem for each “PML” waveguide is solved once for all frequencies and enclosure lengths. The

modal directivity function can then be calculated algebraically. The use of an improved modal basis increases the accuracy of the far-field solution.

At low frequencies, the directivity is governed by the piston mode and greatly affected by the diffraction effects. For an infinitely long enclosure, the beamwidth jumps from π toward an angle that is almost independent of the flange width, followed by a modified inverse-sine-law reduction for about 1 octave. Above this monotonic frequency range, edge diffraction brings “M”-shaped fluctuations in the beamwidth curve, and in this way, the beamwidth asymptotically approaches the $\pi/2$ plateau for an infinite baffle as the flange enlarges. The diffraction effect brought by a finite enclosure length is relatively minor. In the mid- to high-frequency range, where the shape of the horn affects directivity, a preliminary parametric study on classical shapes shows that a parabolic horn exhibits a beamwidth close to a vibrating piston at the mouth over a wide frequency range. The use of a moderate flange could extend the bandwidth of directivity control.

The near-field directivity could be interesting in some applications. To compute it, one may employ a large “PML” waveguide to encompass the observation surface and use the obtained modal solution (see Fig. 7). The near-field directivity function can also be derived from the Kirchhoff–Helmholtz integral²⁰ in a similar way, whereas a closed-form solution is no longer readily available.

The present paper primarily aims to provide valuable insights for the theoretical understanding of radiation of a horn-loaded enclosure through the efficient computation tool, though more general geometries could be modeled with similar procedures, e.g., an axisymmetric enclosure of which the outer profile radius varies along the length.²⁸ In addition, the present modal solutions are also well-suited to the mathematical framework in the authors’ previous work on the theory of maximum directivity.²⁶ It would be interesting to study how the diffraction by a finite enclosure affects the directional beam. Future work could also consider the geometric optimization for the directivity control.

SUPPLEMENTARY MATERIAL

See the supplementary material for further details on the modeling of the external sound field, formulation of the non-axisymmetric directivity function, expressions of the horn shapes, and elucidation for occasional dips in the beamwidth.

ACKNOWLEDGMENTS

This work was partly funded by Le Mans Acoustique in the framework of the Pays de la Loire region. The authors would like to thank the two anonymous reviewers for their helpful comments and suggestions to improve the manuscript.

AUTHOR DECLARATIONS

Conflict of Interest

The authors have no conflicts to disclose.

DATA AVAILABILITY

The data that support the findings of this study are available from the corresponding author upon reasonable request.

¹F. E. Toole, “Music, rooms and listeners: Science in the creation and delivery of audio art,” *Acoust. Today* **9**(2), 36–44 (2013).

²E. G. Williams, *Fourier Acoustics: Sound Radiation and Nearfield Acoustical Holography* (Academic, London, 1999), pp. 15–55.

³T. Mellow and L. Kärkkäinen, “On the sound fields of oblate and prolate hemispheroids in infinite baffles for directivity control,” *J. Acoust. Soc. Am.* **150**(4), 3047–3058 (2021).

⁴T. Mellow and L. Kärkkäinen, “On the sound field of an oscillating disk in a finite open and closed circular baffle,” *J. Acoust. Soc. Am.* **118**(3), 1311–1325 (2005).

⁵T. Mellow, “On the sound field of a resilient disk in free space,” *J. Acoust. Soc. Am.* **123**(4), 1880–1891 (2008).

⁶G. Homicz and J. Lordi, “A note on the radiative directivity patterns of duct acoustic modes,” *J. Sound Vib.* **41**(3), 283–290 (1975).

⁷A. Snakowska and R. Wyrzykowski, “Calculation of the acoustical field of a semi-infinite cylindrical wave-guide by means of the green function expressed in cylindrical coordinates,” *Arch. Acoust.* **11**(3), 261–285 (1986), available at <https://acoustics.ippt.gov.pl/index.php/aa/article/view/3124>.

⁸B. Baddour, P. Joseph, A. McAlpine, and R. Leung, “Acoustic radiation characteristics of cutoff modes from ducts,” *J. Sound Vib.* **541**, 117306 (2022).

⁹S. Morita, N. Kyono, S. Sakai, T. Yamabuchi, and Y. Kagawa, “Acoustic radiation of a horn loudspeaker by the finite element method—A consideration of the acoustic characteristic of horns,” *J. Audio Eng. Soc.* **28**(7/8), 482–489 (1980), available at <http://www.aes.org/e-lib/browse.cfm?elib=3973>.

¹⁰D. J. Henwood, “The boundary-element method and horn design,” *J. Audio Eng. Soc.* **41**(6), 485–496 (1993), available at <http://www.aes.org/e-lib/browse.cfm?elib=6995>.

¹¹Y. Kagawa, T. Yamabuchi, T. Yoshikawa, S. Ooie, N. Kyouno, and T. Shindou, “Finite element approach to acoustic transmission-radiation systems and application to horn and silencer design,” *J. Sound Vib.* **69**(2), 207–228 (1980).

¹²V. Pagneux, N. Amir, and J. Kergomard, “A study of wave propagation in varying cross-section waveguides by modal decomposition. Part I. Theory and validation,” *J. Acoust. Soc. Am.* **100**(4), 2034–2048 (1996).

¹³V. Pagneux, “Multimodal admittance method in waveguides and singularity behavior at high frequencies,” *J. Comput. Appl. Math.* **234**(6), 1834–1841 (2010).

¹⁴J.-F. Mercier and A. Maurel, “Acoustic propagation in non-uniform waveguides: Revisiting Webster equation using evanescent boundary modes,” *Proc. R. Soc. A.* **469**(2156), 20130186 (2013).

¹⁵T. Guennoc, J.-B. Doc, and S. Félix, “Improved multimodal formulation of the wave propagation in a 3D waveguide with varying cross-section and curvature,” *J. Acoust. Soc. Am.* **149**(1), 476–486 (2021).

¹⁶B. Kolbrek and T. Dunker, *High-Quality Horn Loudspeaker Systems: History, Theory and Design* (Kolbrek Elektroakustikk, Rauland, 2019), Chap. 15, pp. 569–599, Chap. 25, pp. 849–850.

¹⁷H. Dong, H. Gao, X. Feng, and Y. Shen, “Shape optimization of acoustic horns for improved directivity control and radiation efficiency based on the multimodal method,” *J. Acoust. Soc. Am.* **149**(3), 1411–1424 (2021).

¹⁸B. Kolbrek and U. P. Svensson, “Using mode matching methods and edge diffraction in horn loudspeaker simulation,” *Acta Acust. united Acust.* **101**(4), 760–774 (2015).

¹⁹S. Félix, J.-B. Doc, and M. A. Boucher, “Modeling of the multimodal radiation from an open-ended waveguide,” *J. Acoust. Soc. Am.* **143**(6), 3520–3528 (2018).

²⁰E. Wadbro, “On the far-field properties of an acoustic horn,” Report No. 2006-042, Department of Information Technology, Uppsala University (2006).

²¹W. Magnus, F. Oberhettinger, and R. P. Soni, *Formulas and Theorems for the Special Functions of Mathematical Physics*, (Springer Science & Business Media, 2013), Vol. **52**, p. 79.

²²The Neumann modes are given here as a standard approach. We use the IMAM with an improved modal basis to compute $v_z(r', 0)$ more efficiently (see Sec. IIC).

²³G. Gabard and R. J. Astley, “Theoretical model for sound radiation from annular jet pipes: Far- and near-field solutions,” *J. Fluid Mech.* **549**, 315–341 (2006).

²⁴A. Snakowska and J. Jurkiewicz, “Efficiency of energy radiation from an unflanged cylindrical duct in case of multimode excitation,” *Acta Acust. united Acust.* **96**(3), 416–424 (2010).

²⁵L. Beranek and T. Mellow, *Acoustics: Sound Fields, Transducers and Vibration*, 2nd ed. (Academic Press, London, 2019), pp. 463–510, 659–683.

²⁶H. Dong, J.-B. Doc, and S. Félix, “Maximum directivity of flanged open-ended waveguides,” *J. Acoust. Soc. Am.* **154**(1), 115–125 (2023).

²⁷D. B. Keele, Jr., “Loudspeaker horn,” U.S. patent 4,308,932 (January 5, 1982).

²⁸T. Guennoc, “Modélisation du rayonnement des guides de forme complexe par une méthode multimodale” (“Modeling the radiation of complex shaped guides using a multimodal method”), Ph.D. thesis, Le Mans, 2021.